International Journal of Hydrogen Energy 60 (2024) 468–478

Contents lists available at ScienceDirect

International Journal of Hydrogen Energy

journal homepage: www.elsevier.com/locate/he

Experimental study on the effect of hydrogen on the mechanical properties of hulett sandstone

Ehsan Dabbaghi [a], Kam Ng [b,*], Tyler C. Brown [c], Ying Yu [c]

[a], Department of Civil and Architectural Engineering and Construction Management, University of Wyoming, Laramie, WY, USA
[b], Department of Civil and Architectural Engineering and Construction Management, 1000 E. University Ave, University of Wyoming, Laramie, WY, USA
[c] Center for Economic Geology Research, School of Energy Resources, University of Wyoming, Laramie, WY, USA

ARTICLE INFO

Handling Editor: Prof. J. W. Sheffield

Keywords:
Underground hydrogen storage
Saline aquifer
Rock mechanics
Rock-fluid interactions
Mechanical properties
Laboratory tests

ABSTRACT

One of the challenges of storing hydrogen in saline aquifers is the possible geochemical reactions between host rock, formation solution, and hydrogen. This study investigated the effect of hydrogen treatment on the mechanical properties of sandstone samples from Hulett member of Sundance Formation, a potential underground hydrogen storage host in Wyoming, USA. Cylindrical specimens were treated with brine, brine+50%H_2, and brine+100%H_2 for two weeks at a pressure of 15 MPa and a temperature of 83 °C. X-ray diffraction (XRD), scanning electron microscope (SEM), Brunauer-Emmett-Teller (BET), uniaxial compression, and triaxial compression tests were conducted on specimens. Results showed that specimens treated with brine+50%H_2 and brine+100%H_2, on average, exhibited 24 and 41% lower peak strength, respectively, compared to that of specimens treated with the brine. XRD results showed a decrease in dolomite and clay content of specimens after exposure to hydrogen, causing degradation of the mechanical and elastic properties of the specimens.

1. Introduction

The increase in world population, industrialization, and individual income have contributed to the rising energy demand and consumption. It is estimated that there will be a 25% increase in energy demand by 2050 [1]. Although fossil fuels have had the largest share of the global energy mix for decades (presently about 80%), the depletion of nonrenewable resources, the impact of geopolitical uncertainties, and negative environmental consequences due to fossil-fuel utilization have inevitably demanded more sources of clean and renewable energy. One solution to this problem is to increase the use of renewable energies, such as geothermal, hydro, wind, and solar. Renewable energies are predicted to provide 45% of all the needed energy by 2050 [2], in accordance with the goal set by the International Energy Agency (IEA) to reach net zero emissions [3]. However, a potential challenge with these sources of energy is that seasonal changes and geographical constraints can disrupt their production and usage [4]. Energy from hydrogen, on the other hand, can be produced and used all year round.

Hydrogen is the lightest and most abundant element, and its high energy density makes it a desirable alternative to fossil fuels. Hydrogen can be produced from low carbon energy (green hydrogen), iron-rich rock formation (orange hydrogen), carbon fuel (brown hydrogen), natural gas without CO_2 capture (grey hydrogen), and natural gas with CO_2 capture and storage (blue hydrogen) [5]. In 2020, hydrogen and hydrogen-based fuels were less than 0.1% of the total final energy consumption. However, hydrogen could provide 10% of the total fine energy consumption by 2050 according to the IEA [6]. As an important surplus energy, hydrogen needs to be stored for later use. Tanks and cylinders are the short-term storage options. However, their low storage volume and high energy demands require a long-term storage solution [7].

Geological storage is an efficient and low-cost option for storing large volumes of hydrogen. Depleted oil and gas reservoirs, salt caverns, coal seams, and saline aquifers can be used for storing hydrogen since they provide large volumes of space [8]. Among the geological storage options, saline aquifers are considered the most cost-effective for underground hydrogen storage (UHS) [9]. One potential benefit of using saline aquifers is that the salt decreases hydrogen solubility in water, thus limiting hydrogen dissolution which would be considered a net resource loss [7]. Since small molecules of hydrogen can easily diffuse into different parts of the formation rock [4], it is necessary to study the heterogeneity inherent to natural underground reservoirs in order to mitigate gas loss during UHS. Previous studies that simulated UHS conditions showed that lower injection rates and the presence of a

* Corresponding author.
E-mail addresses: edabbagh@uwyo.edu (E. Dabbaghi), kng1@uwyo.edu (K. Ng), tbrown46@uwyo.edu (T.C. Brown), yyu3@uwyo.edu (Y. Yu).

https://doi.org/10.1016/j.ijhydene.2024.02.210
Received 7 December 2023; Received in revised form 14 February 2024; Accepted 16 February 2024
Available online 21 February 2024
0360-3199/© 2024 Hydrogen Energy Publications LLC. Published by Elsevier Ltd. All rights reserved.

caprock both improved hydrogen recovery rates from a heterogenous sandstone reservoir [10]. For an injection rate of 360 kg/h, the recovery rates increased from 29.9% to 36% through the addition of a caprock. A higher injection rate of 18,000 kg/h drastically reduced recovery rates both with (7%) and without (4.9%) a caprock. Simulations of hydrogen injection into the depleted Haynesville shale-gas formation were conducted by Singh [11] for three durations: short-term (6 h of injection followed by 6 h of production, total 60 cycles), intermediate-term (15 days of injection followed by 15 days of production, total 18 cycles), and long-term (60 days of injection followed by 60 days of production, total 10 cycles). Results showed that increasing the duration of cycles from short-term to long-term improved hydrogen recovery from 44.7% to 71%; longer cycles, however, did reduce produced hydrogen purity. Further, decreasing the permeability (K) of the formation from 0.01 mD to 0.001 mD improved hydrogen recovery by 14.7%, but also decreased purity by 50%. These studies illustrate how important understanding the interactions between hydrogen, rock, and the formation water is because those interactions can significantly impact the mineral composition, matrix, elastic, and mechanical properties of the rock.

Some studies have been conducted to investigate the geochemical reactions between rocks and hydrogen. Truche et al. [12] reported rapid sulfide production (2.5 mM) in the first 48 h when hydrogen (10% content), with a relative pressure of 0.6 MPa at a temperature of 250 °C, was introduced into an autoclave containing sieved claystone samples. Batch experiments on 30–50 mm plugs of Permian Sandstone under reservoir conditions (20 MPa, 120 °C, 35% salinity) did not show any reactions with hydrogen except that the host brine turned brown after the batch experiments [13]. In another study, batch experiments on sandstone and siltstone samples showed the dissolution of anhydrite and carbonate cement after only six weeks of hydrogen treatment at 10–20 MPa and 40–130 °C [14]. Despite the dissolution of these minerals in all sample types, there was no clear relationship with the development of porosity (φ), even though there was a recorded increase in sample surface area. In another series of batch experiments on sandstone samples, Pudlo et al. [15] observed the dissolution of sulfate and calcite, but no change in the volume of the silicate phase after exposure to hydrogen at 40–120 °C and 4–20 MPa. In all experiments, if anhydrite, barite, or calcite were absent, then no significant geochemical reaction was observed. These minerals acted as cementation and pore-filling materials, and their dissolution led to an increase in φ and K. Buntsandstein sandstone samples showed an increase in recrystallized muscovite content after treatment with pure hydrogen at dry conditions; under 10 MPa and 100 °C for six months [16]. In another set of batch experiments, Hassanpouryouzband et al. [17] reported the disaggregation of different sandstone samples with particle sizes between 0.355 and 4 mm, and an increase in both calcium (43 ppm) and potassium (19 ppm) contents after 1–8 weeks of hydrogen treatment at 1–20 MPa and 60–80 °C. To determine the effect of chemical reactions between calcite, hydrogen, and water, Gelencsér et al. [18] conducted batch experiments on powdered natural pure calcite (Iceland spar) under a cell pressure of hydrogen or nitrogen at 10 MPa, 105 °C and reaction times of 3, 24, and 72 h. Inductively coupled plasma optical emission spectroscopy (ICP-OES) results showed almost no difference in the amount of dissolved calcite after either hydrogen or nitrogen injection. Our review of the current literature shows that the reactions between hydrogen and rock depend on other factors like temperature, pressure, duration of the experiment, and rock minerals.

Although previous studies investigated the effect of hydrogen injection on the mineral content of rocks, experimental studies are rarely conducted to understand the effect of hydrogen-rock interactions on the mechanical and elastic behaviors of rocks. This paper investigates the effect of rock-brine-hydrogen interactions on the mineralogy, pore structure, and elastic and mechanical properties of Hulett Sandstone samples collected in the Powder River Basin, Wyoming, USA. This study is potentially the first of its kind to present changes in the mechanical and elastic properties of the rock after hydrogen treatment through a series of uniaxial and triaxial compression tests, microstructural analysis, and mineral characterization. The practicality and safety of UHS require knowing the implications of hydrogen injection on underground geologic formations.

2. Geological description of Hulett sandstone

This study focuses on subarkosic sandstone samples from the Jurassic Hulett member of the Sundance Formation collected from Wyoming CarbonSAFE PRB#1 well in the Powder River Basin, Wyoming, USA. At the location of the well, the top of the Hulett sandstone is 2522 m below the surface and is 25 m thick. The mean φ and K of sidewall cores from the Upper Sundance Members and the adjacent Morrison Formation are 3.92% and 600 nD under 34.5 MPa net confining pressure, respectively. Based on the log and seismic data, the studied site is relatively flat and continuous [19]. The hydrostatic pressure gradient at the studied site was estimated from the Modular Dynamic Tester (MDT) log to be 0.009 MPa/m, which is considered "under pressured" [20]. The formation water consists of: NaCl: 82 g/L, KCl: 9.515 g/L, Na_2SO_4: 7.631 g/L, $CaCl_2 \bullet 2H_2O$: 4.658 g/L, and $NaHCO_3$: 1.09 g/L. The temperature gradient was estimated to be 0.0328 °C/m. In addition, the total dissolved solids (TDS) of brine were analyzed at 104,020 mg/L.

Six samples were obtained from the upper Hulett member at depths of 2522.5 m, 2522.8 m, 2523.1 m, 2524.4 m, 2525.0 m, and 2525.2 m. Fig. 1 shows thin-section images [19] of samples proximal to the depths sampled in this study. Even though all of the samples are within 3 m, heterogeneity is obvious. Deeper samples (2524.6 and 2525.7 m) show larger grain sizes, higher φ, and higher K than those from shallower depths (2522.4 and 2522.7 m), and previous work by Quillinan et al. [19] noted some mineral complexity despite structural consistency throughout the region. The thickness of the Hulett Sandstone, its basal and overlying caprock seals [21–23], and its under-pressure nature ([20]; Y. [24]) all suggest a viable deep saline aquifer that might be suitable for UHS. Thus, this experimental study is indispensable to understand the effect of hydrogen storage on the mineralogy and mechanical properties of the Hulett sandstone.

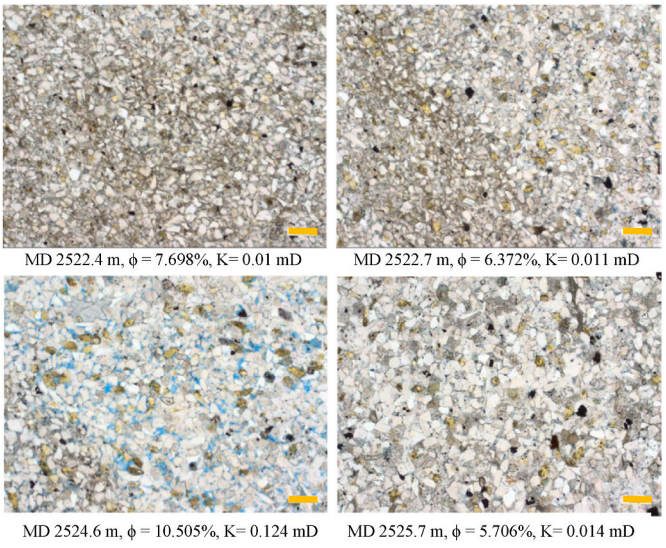

Fig. 1. Thin section images from the Hulett Sandstone. MD stands for median depth, φ stands for porosity, and K stands for gas permeability, after [19]. The orange scale bar is 500 μm. (For interpretation of the references to colour in this figure legend, the reader is referred to the Web version of this article.)

3. Experimental methods

3.1. Specimen preparation

Sandstone samples with a 102-mm core diameter were acquired from the UW-PRB#1 library. Using a wet coring drill, specimens with diameters of 25 and 38 mm were cored out of the original samples. Specimens were then cut to a length double their diameters using a wet saw, in accordance with ASTM D5453-19. A surface grinder was then used to bring both ends of the specimen perpendicular to its sides. Each specimen was then placed in the Soxhlet extractor, where a mixture (1:1) of methanol and Toluene was circulated through the specimen for 24 h so that the salt and oil from the original drilling could be extracted. Finally, the specimens were dried in an oven at 105 °C for 24 h.

3.2. Rock treatments

Three treatment conditions were applied to the rock specimens. The first treatment condition, "0%H_2", submerged the specimen in the brine solution (composition discussed in Section 2) using a vacuum incubator for one week at room temperature. In the second treatment condition, "50%H_2", rock specimens were submerged in brine for one week (same as the 0%H_2 treatment condition). Next, it was transferred to a high pressure and high temperature (HPHT) autoclave vessel (MTI HPV10LH) (Fig. 2a) filled with 75-mm height brine (Fig. 2b). The HPHT vessel has a capacity of 10 L, and can hold up pressure up to 20 MPa, and heating limit of 200 °C. Using a gas booster (Maximator DLE 75), the pressure from a gas tank containing 50% hydrogen and 50% argon (99.999% purity) was increased and transferred to the vessel (Fig. 2a). The inlet valve was opened, and the gas injection process started until the pressure inside the vessel reached 15 MPa, as indicated by the vessel's pressure gauge. Next, the inlet valve was closed so that the pressure would be sustained in the vessel. At this point, the vessel's oven was turned on to raise the vessel temperature to 83 °C. The treatment pressure and temperature were chosen based on the in-situ formation condition. The specimen was kept in the vessel for 336 h (two weeks). The third treatment condition known as 100%H_2 was the same as the 50%H_2 treatment condition except 100% hydrogen (99.999% purity) was injected into the vessel for treatment.

3.3. Rock characterization

X-ray diffraction (XRD) tests were conducted on powdered rock specimens using the Rigaku SmartLab SE X-ray Diffractometer in the University of Wyoming's Materials Characterization Laboratory. All powdered samples were analyzed using a voltage of 44 kV and a current of 44 mA, from 5 to 80° 2θ, at a scan rate of 4°/min. After these analyses, oriented clay mounts (procedure outlined by Ref. [25]), were analyzed at 2θ ranging from 3° to 32°, at a rate of 3°/min before and after treatment with ethylene glycol (used to indicate the presence of swelling clay minerals). Finally, the intensity versus different 2θ values were plotted to determine different minerals. For quantification of the results, raw XRD data were fed to MDI Jade software (Materials Data Inc., Liverpool, CA), and percentage weights of all the possible phases were acquired. The Jade software calculates the peak area assigned to each individual phase to quantify the percentage weights.

Flat chips extracted from the specimens were gold-coated and analyzed using the FEI Quanta 250 Scanning Electron Microscope. Accelerating voltages of 5 and 20 kV and a spot size of 3 were used in the SEM tests. The INCA software was used to perform the Energy dispersive X-ray spectroscopy (EDS) to detect the different elements and minerals of each specimen.

Thin sections were prepared from cylindrical specimens. Void spaces on the specimens' surfaces were stained with blue epoxy (e.g., Fig. 1).

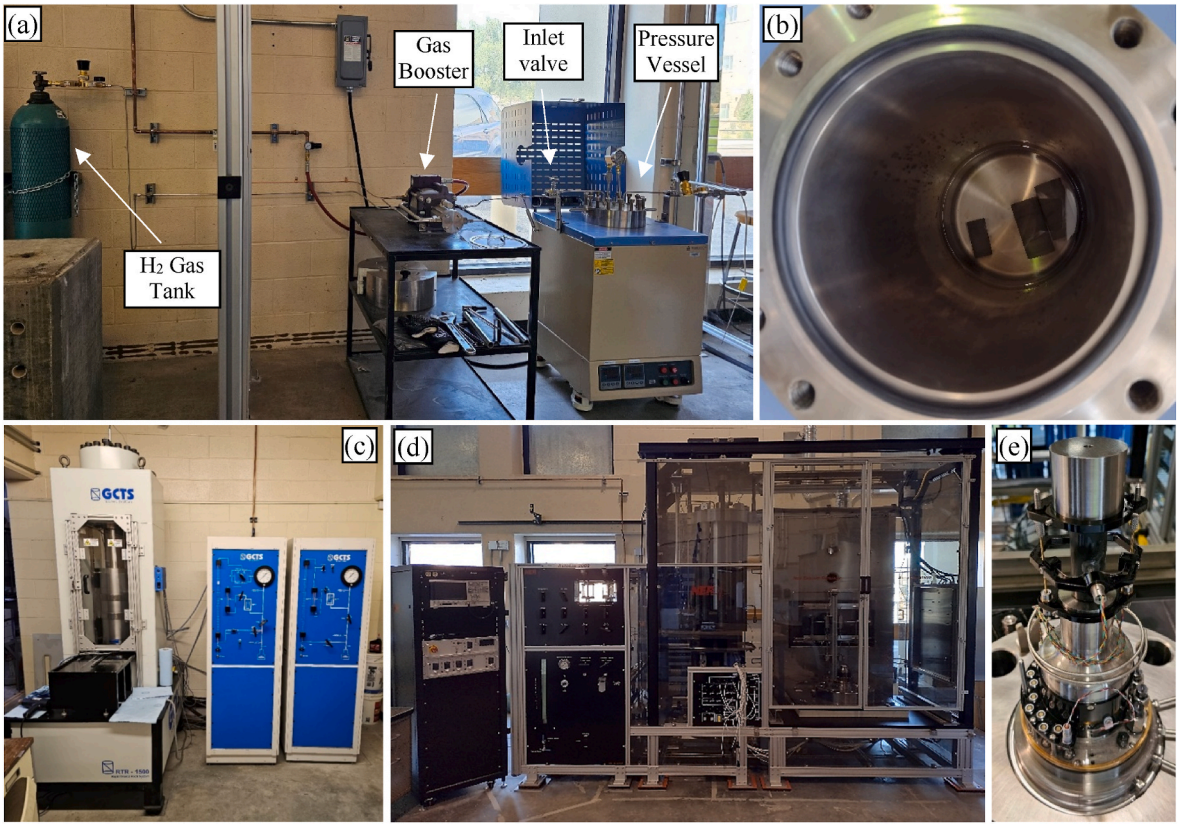

Fig. 2. Photos show a) the high-pressure and high-temperature vessel for hydrogen treatment, b) rock specimens submerged in the brine inside the vessel before treatment, c) GCTS equipment, d) NER equipment, and e) the picture of a rock specimen setup for the TC test.

An Epson scanner was used to scan the thin sections and provide the digital image. The software GeoPixelCounter v. 1.0 by Mock et al. [26] was used to count the number of pixels of different parts (grains and voids) that make up the surface of the specimen to determine the φ.

For the Brunauer-Emmett-Teller (BET) test, small chips (less than 1 cm wide) extracted from the specimens were placed in test tubes and dried at 105 °C for 24 h while Helium was purged into them. Next, the test tubes containing the specimens were placed in the Micromeritics TriStar 3000 equipment in a Nitrogen gas environment for measuring the surface area and pore size distribution of the specimens.

3.4. Uniaxial and triaxial compression tests

Table 1 summarizes the specimen identification, rock porosity, treatment condition, confining pressure, pore pressure, and temperature for mechanical experiments consisting of uniaxial compression (UC) and triaxial compression (TC) tests. For each treatment condition, three rock specimens were prepared for one UC test and two TC tests. Two confining pressures of 43 and 63 MPa and pore pressure of 23 MPa were used in the TC tests. All experiments were conducted at the in-situ temperature of 83 °C. Noteworthy to mention that because of the inherent heterogeneity of the specimens, rock specimens with two φ values of 6.4 and 10.5% were considered. Since the specimens treated with 0%H_2 at φ of 6.4% were different from those specimens treated with 100%H_2 at φ of 10.5%, three specimens with the φ of 10.5% were prepared using the first treatment condition for UC and TC tests to account for the effect of φ. Each specimen ID consists of two parts: 1) the specimen number (from S1 to S12), and 2) the treatment and test conditions in parenthesis. The treatment conditions are 0H for specimens submerged in brine, 50H for specimens treated with 50%H_2, and 100H for specimens treated with 100%H_2. The mechanical testing conditions are UC for the uniaxial compression test, TC20 for the triaxial compression test with an effective confining pressure of 20 MPa, and TC40 for the triaxial compression test with an effective confining pressure of 40 MPa.

UC tests were conducted on 25-mm diameter specimens using the GCTS RTR-1500 equipment (Fig. 2c) at the University of Wyoming (UW). Each rock specimen was covered with heat shrink tubing and instrumented with one radial and two axial LVDTs. A sitting deviatoric stress of about 0.5 MPa was applied to the specimen so that the loading process would be smooth and controlled. Next, the deviatoric stress was increased at a loading rate of 1% axial strain per minute until failure. Failure was defined by a continuous decrease in the axial stress after reaching the peak point in the stress-strain plot. TC tests were performed on 38-mm diameter specimens using the NER AutoLab 3000 equipment (Fig. 2d) at the UW. The specimen was placed inside a Viton jacket between two core holders and instrumented with one radial and two axial LVDTs (Fig. 2e).

Fig. 3 shows an example of a TC test procedure. An initial confining pressure of 2 MPa was applied to the specimen (stage 1). The oven of the equipment was connected, and the target temperature was set to 83 °C (stage 2). After reaching the target temperature, the confining pressure was increased to 5 MPa (stage 3). At this point, a pore water pressure of 2 MPa was applied to the specimen (stage 4). Next, both the confining and pore pressures were ramped up to their target values at a rate of 3 MPa/min (stage 5). After that, an initial deviatoric stress of 2 MPa was applied to the specimen (stage 6). Finally, the deviatoric stress was increased at a rate of 0.003 mm/s until post-failure was observed (stage 7). It is worth noting that the temperature was kept constant at 83 °C throughout the tests.

Table 1
Summary of the specimen IDs, treatment conditions, and mechanical testing conditions.

Specimen ID	φ (%)	Treatment Condition	Confining Pressure (MPa)	Pore Pressure (MPa)	Temperature (°C)
S1 (0H-UC)	6.4	Submerged in Brine for one week	0	0	83
S2 (0H-TC20)			43	23	
S3 (0H-TC40)			63	23	
S4 (0H-UC)	10.5	Submerged in Brine for one week	0	0	
S5 (0H-TC20)			43	23	
S6 (0H-TC40)			63	23	
S7 (50H-UC)	10.5	Submerged in Brine for one week + treated with 50%H_2 for two weeks	0	0	
S8 (50H-TC20)			43	23	
S9 (50H-TC40)			63	23	
S10 (100H-UC)	10.5	Submerged in Brine for one week + treated with 100%H_2 for two weeks	0	0	
S11 (100H-TC20)			43	23	
S12 (100H-TC40)			63	23	

4. Results and discussion

4.1. Characterization

4.1.1. X-ray diffraction (XRD)

Fig. 4 shows the XRD patterns, and Table 2 summarizes the mineral composition by weight percent for the three different treatment conditions. Quartz is the main phase in all three specimens despite the different treatment conditions. Results indicate that quartz, anorthite, albite, and microcline contents are all higher in the specimens treated with H_2 than in the brine-submerged specimen. To be clear, the higher relative weight percents of these minerals are not due to precipitation, rather the increase is attributed to the reduction in dolomite, ankerite, and clay minerals from H_2 treatment. Dolomite, ankerite, and clay mineral content decrease from 50%H_2 to 100%H_2 treatment. Although clay content decreased after hydrogen treatment, illite remained the main clay-mineral phase in each specimen, and smectite was minor.

The reduction in dolomite most likely resulted from dissolution described by Eq. (1) [27], where the dolomite, $CaMg(CO_3)_2$, reacts with H_2 to produce calcite, magnesium hydroxide, methane, and water.

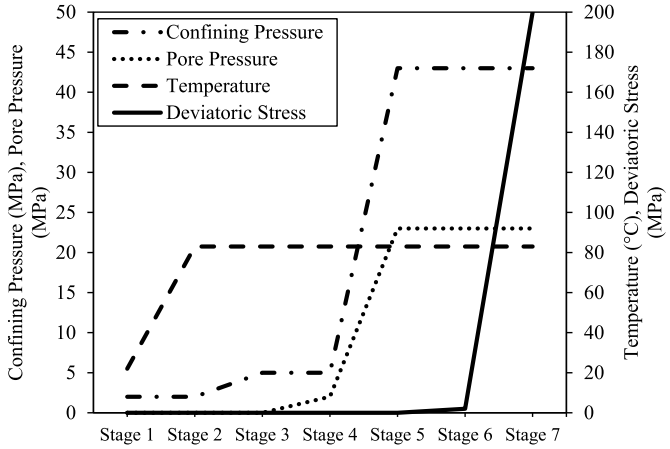

Fig. 3. An example of the steps and timeframe of the TC tests under 43 MPa of confining pressure and 23 MPa of pore pressure.

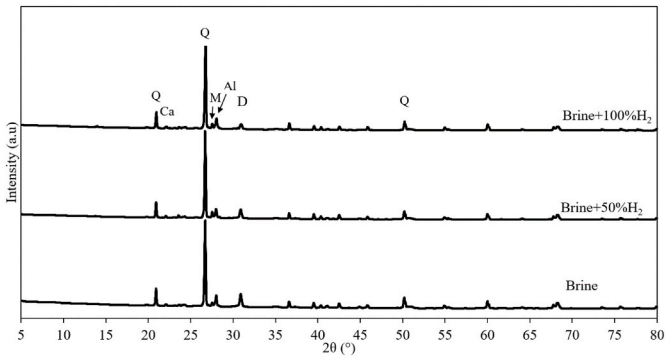

Fig. 4. XRD patterns of specimens with three different treatment conditions (Q = Quartz; Al = Albite; D = Dolomite; M = Microline; Ca = Calcite).

$$4H_2 + CaMg(CO_3)_2 \rightarrow CaCO_3 + Mg(OH)_2 + CH_4 + H_2O \quad (1)$$

The dissolution of illite explains the reduction in the clay content after the hydrogen treatment. There is a high interfacial tension (IFT) between clay and hydrogen that makes a reaction between them unlikely [4]. However, the reaction between illite and water leads to the dissolution of illite as described in Eq. (2) [28]:

$$K_{0.6}Mg_{0.25}Al_{2.3}Si_{3.5}O_{10}(OH)_2 + 11.2H_2O \rightarrow 0.6K^+ + 0.25Mg^{2+} + 2.3Al(OH)^{4-} + 3.5H_4SiO_4 + 1.2H^+ \quad (2)$$

After treatment, the pH values of the 0%H_2, 50%H_2, and 100%H_2 solutions were measured at 6.5, 6.9, and 7.6, respectively. The increase in the pH of the solutions containing H_2 shows that the intensity of the chemical reaction increases when the H_2 concentration increases from 0% to 100%. The dissolution and precipitation of carbonates are likely the cause of the increase in pH [29].

Along with monitoring the changes in the minerals of specimens, future studies can also measure the composition of saturation fluid before and after treatment with hydrogen to get a more comprehensive understanding of the chemical changes.

4.1.2. Scanning electron microscopy (SEM)

Fig. 5a–c shows SEM images of the selected specimens treated with 0%H_2, 50%H_2, and 100%H_2, respectively. Fig. 5a shows that the quartz grains are surrounded by dolomite grains, and it can be deduced that dolomite plays a role in the cementation of the quartz grains. Most of the pores are smaller than 5 μm. Fig. 5b shows that the dolomite mineral concentration has reduced due to the moderate dissolution of dolomite after 50%H_2 treatment. In addition, the negligible small amount of calcite ($CaCO_3$) produced from the moderate dolomite dissolution reaction could not be determined in Fig. 5b. Furthermore, the minerals in Fig. 5b are less compacted with most pores smaller than 10 μm. Fig. 5c shows that the surface of the specimen is smoother than the two other specimens, and dolomites are mostly dissolved by the 100%H_2 to form calcite. The pores are smaller than 10 μm, and the precipitated calcites are widely observed. It is believed that the precipitated calcite grains might have covered or filled some of the bigger pores. The severe dolomite dissolution and precipitation of calcite resulting from the reaction with 100%H_2 could have changed the original microstructure and cementation of the sandstone.

4.1.3. Porosity estimates using thin sections

Thin section images of selected specimens treated with 0%H_2 (Fig. 6a), 50%H_2 (Figs. 6b), and 100%H_2 (Fig. 6c) are shown with blue-epoxy-impregnated pore space. GeoPixelCounter [26] shows an increase in porosity from 14.7% in the specimen treated with 0%H_2, to 19.4% in the 50%H_2 treatment, to 37.7% in the 100%H_2 treatment. This might suggest that H_2 treatment increases relative porosity, but it could also reflect rock heterogeneity. As discussed in Section 2, previous studies had a maximum of 10.5% porosity for samples from depths comparable to those in this study. The higher baseline porosity in the 0%H_2 specimen could either reflect heterogeneity or the different measuring methods.

4.1.4. BET

Table 3 summarizes BET measurements of the surface area, cumulative volumes of mesopores (with a diameter of 2–50 nm), macropores (with a diameter >50 nm), and total pores of the rock specimens with three treatment conditions, along with the respective changes in pore volumes from brine treatment to hydrogen treatments. The specimens treated with 0%H_2, 50%H_2, and 100%H_2 have surface areas of 9.31, 9.16, and 10.78 m^2/g, respectively, and 100%H_2 treatment increases the surface area by about 16%, compared to the specimen treated with 0% H_2. The cumulative mesopore volumes of specimens treated with 0%H_2, 50%H_2, and 100%H_2 are 0.156, 0.187, and 0.176 cm^3/g, respectively. The cumulative macropore volumes of specimens treated with 0%H_2, 50%H_2, and 100%H_2 are 0.054, 0.046, and 0.055 cm^3/g, respectively. This suggests that mesopores constitute the majority of pore volumes in all samples. The total pore volumes of specimens treated with 0%H_2, 50%H_2, and 100%H_2 are 0.21, 0.233, and 0.231 cm^3/g, respectively. The increase in the total pore volume reveals the effect of H_2 on the microstructure of Hulett sandstone. Pore volumes obtained by BET are more reliable than the estimates made from thin section images (section 4.1.3) since porosity measured in thin section images is from a two-dimensional slice and not the representative three-dimensional volume measured by BET.

4.2. Confinement stage

4.2.1. Volumetric stress-strain responses

Fig. 7a shows the changes in volumetric strain (ε_v) versus the effective confining pressure for the four specimens with three treatment conditions and under a target confining pressure (P_c) of 43 MPa and pore pressure (P_p) of 23 MPa. The ε_v was calculated using the radial strain (ε_r) and axial strain (ε_a), given by Eq. (3)

$$\varepsilon_v = 2\varepsilon_r + \varepsilon_a \quad (3)$$

Effective confining pressure or differential pressure (P_d) was calculated as the difference between P_c and P_p given by Eq. (4)

$$P_d = P_c - P_p \quad (4)$$

Fig. 7a shows that specimen S11 (100H-TC20) exhibits the lowest ε_v, while specimen S5 (0H-TC20) experiences the highest ε_v. This comparison shows that 100%H_2 treatment made specimen S11 less compressible, with 80% smaller maximum ε_v than that of specimen S5. We believe that the relatively higher final porosity of the S11 specimen, as suggested in Section 4.1.3 based on thin sections and assuming more connected pores, facilitates the buildup of target P_p inside the pore spaces, accelerates reaching the P_d equilibrium, and hence contributes

Table 2
Relative mineral weight percents at three different treatment conditions.

Treatment	Quartz	Dolomite	Ankerite	Anorthite	Albite	Microline	Clay + Phyllosilicates
0%H_2	58.4	13.0	3.5	0.6	11.2	0.0	13.3
50%H_2	61.8	10.4	1.3	2.2	13.0	2.8	8.4
100%H_2	71.7	5.9	2.6	2.7	11.8	3.0	1.9

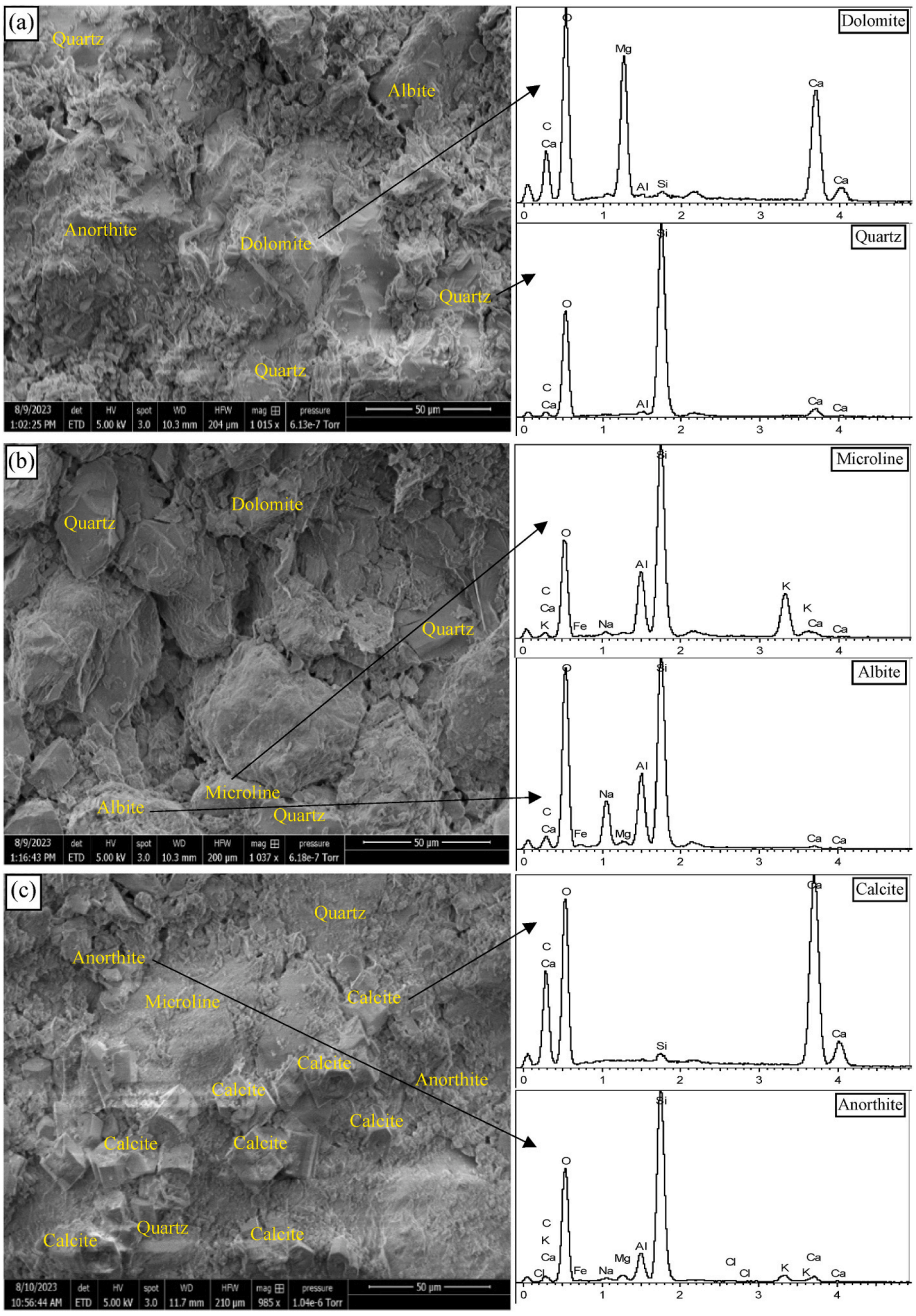

Fig. 5. SEM images of selected specimens treated with a) 0%H_2, b) 50%H_2, and c) 100%H_2.

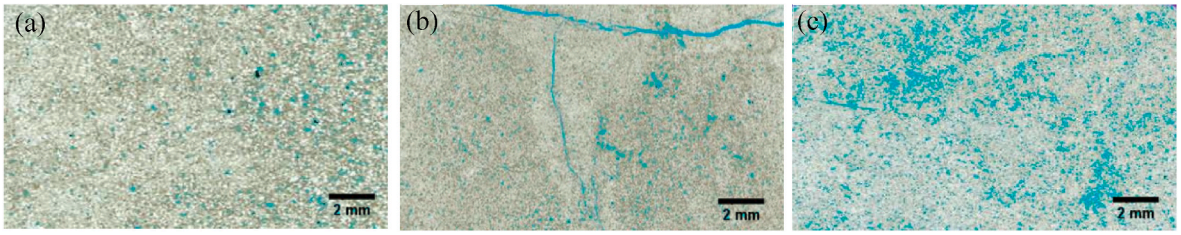

Fig. 6. Scanned images of thin sections of specimens treated with a) 0%H_2, b) 50%H_2, and c) 100%H_2. Blue indicates pore space. (For interpretation of the references to colour in this figure legend, the reader is referred to the Web version of this article.)

to a lower ε_v during the confining stage. On the other hand, specimen S8 (50H-TC20) exhibits a higher ε_v than specimen S2 (0H-TC20) until the P_d reaches 10 MPa, but the difference in the ε_v begins to diminish at $P_d >$ 10 MPa. It is believed that the P_p begins building up inside the specimen's pores, countering the compression from the P_c. At the end of the confining stage, the ε_v of specimen S8 (50H-TC20) becomes comparable

Table 3
BET test results of rock specimens subjected to three treatment conditions.

Treatment	Surface Area		Mesopore volume		Macropore volume		Total pore	
	Value (m^2/g)	Change (%)	Value (cm^3/g)	Change (%)	Value (cm^3/g)	Change (%)	Value (cm^3/g)	Change (%)
0%H_2	9.3077	–	0.156	–	0.054	–	0.21	–
50%H_2	9.1645	−1.53	0.187	19.87	0.046	−14.81	0.233	10.95
100%H_2	10.7765	15.78	0.176	12.82	0.055	1.85	0.231	10

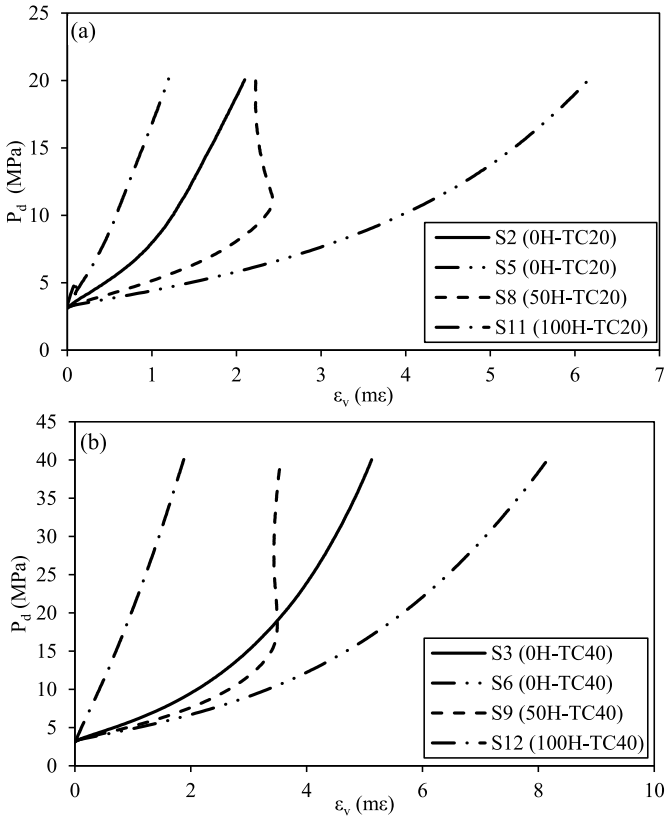

Fig. 7. The relationship between volumetric strain (ε_v) and the effective confining pressure (P_d) for four rock specimens under a target effective pressure of a) 20 MPa and b) 40 MPa.

to that of specimen S2 (0H-TC20). For specimens treated with 0%H_2, the specimen S5 (0H-TC20) with a higher initial φ of 10.5% experiences a higher ε_v than that of the specimen S2 (0H-TC20) with a lower initial φ of 6.4%. We believe that specimen S5 may have more isolated pores that prevent the buildup of P_p in the pore spaces and for this, it experiences higher compression in the pore spaces than that in specimen S2.

Fig. 7b shows the changes in ε_v versus the P_d for the four specimens with different treatment conditions tested under a higher target P_c of 63 MPa and P_p of 23 MPa. Similar to Fig. 7a, for the same initial φ of 10.5%, the specimen S6 (0H-TC40) exhibits the highest ε_v while the specimen S12 (100H-TC40) experiences the smallest maximum ε_v or 76% smaller in ε_v. The treatment with 100%H_2 increases the final φ, facilitates the building up of P_p in pore spaces, and hence, reduces the compressibility of the specimen. For the same initial φ of 6.4%, specimen S9 (50H-TC40) shows higher ε_v than that of specimen S3 (0H-TC40) until the P_d reaches about 19 MPa. It is believed that the water reaching the pores of the specimen and the P_p builds up inside the specimen counter the continuous increase in ε_v from the P_c application. At the end of the confining stage, the specimen S9 (50H-TC40) shows a 31% smaller ε_v than that of the specimen S3 (0H-TC40). For treatment with 0%H_2, specimen S6 (0H-TC40) with a higher initial φ of 10.5% exhibits a larger ε_v than that of specimen S3 (0H-TC40) with a lower initial φ of 6.4%. This observation agrees with the P_d-ε_v responses of specimens subjected to P_d of 20 MPa in Fig. 7a.

Comparing the P_d-ε_v responses in Fig. 7a and b, both specimens S8 (50H-TC20) and S9 (50H-TC40) experience unusual P_d-ε_v responses with an initial increase in ε_v with P_d followed by a decrease in ε_v before reaching the target P_d. Increasing the P_d from 20 to 40 MPa increases the maximum ε_v of the specimens S2 (0H-TC20) and S3 (0H-TC40) at the initial φ of 6.4% from 2.1 mε to 5.1 mε or 143%. However, the specimens S5 (0H-TC20) and S6 (0H-TC40) with the higher initial φ of 10.5% experience a smaller increase in ε_v from 6.1 to 8.16 mε or 34% when the P_d increases from 20 to 40 MPa. For treatment with 50%H_2, the ε_v increases from 2.2 to 3.5 mε or 59% when the P_d increases from 20 to 40 MPa. At P_d of 20 MPa, specimen S8 (50H-TC20) has the maximum ε_v comparable to that of specimen S2 (0H-TC20) but at P_d of 40 MPa, the maximum ε_v of specimen S9 (50H-TC40) has a value 32% lower than that of the specimen S3 (0H-TC40). It is believed that the effect of hydrogen treatment on the specimens at a higher P_d is more significant, compared to a lower P_d. Lastly, the specimens S11 (100H-TC20) and S12 (100H-TC40) exhibit an increase in the maximum ε_v from 1.2 to 1.9 mε or 58% with the increase in P_d from 20 to 40 MPa.

4.2.2. Bulk modulus

Bulk Modulus (K) as an indicator of the change in the volume of the specimen at the confining stage was calculated using Eq. (5)

$$K = \frac{\Delta P_d}{\Delta \varepsilon_v} \tag{5}$$

where, ΔP_d is the changes in effective confining pressure, and $\Delta\varepsilon_v$ is the changes in volumetric strain.

Fig. 8 shows the increase in K with an increase in P_d for the three treatment conditions and two initial φ values during the confinement stage. Specifically, the increase in the P_d from 20 to 40 MPa increases the K of specimens treated with 0%H_2 with the initial φ of 6.4% by 10%. The specimens treated with 0%H_2 with a higher initial φ of 10.5% exhibit a much higher increase in K by about 65%. Increasing the P_d from 20 to 40 MPa increases the K values by 36% and 17% of the specimens treated with 50%H_2 and 100%H_2, respectively. The specimens treated with 100%H_2 exhibit the highest K values at both P_d values or 4.3 times higher than those of the specimens treated with 0%H_2 at the same initial

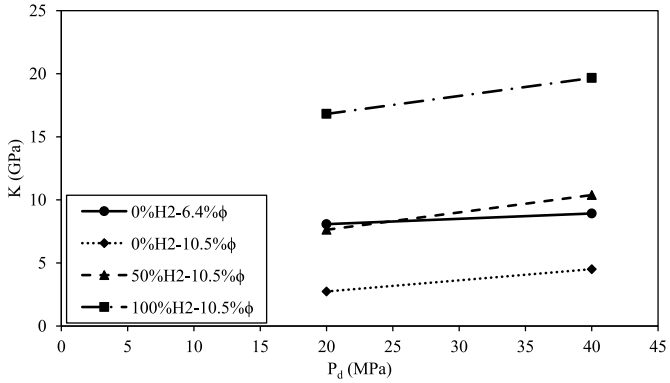

Fig. 8. Changes in bulk modulus (K) versus the effective confining pressure (P_d) for all the specimens tested under triaxial conditions.

φ of 10.5%. On the other hand, the specimens treated with 50%H_2 have a K comparable to that of the specimen treated with 0%H_2 with φ of 6.4%. Lastly, the specimens treated with 0%H_2 with φ of 10.5% exhibit the lowest average K of 3.6 GPa. K depends on the stiffness of mineral grains, and hence, specimens treated with 100%H_2 containing the highest quartz content and lowest clay content exhibit the highest K. Accordingly, specimens treated with 50%H_2 and 0%H_2 exhibit medium and lowest K values, respectively.

4.2.3. Relationship between microstructure and mechanical behavior in confining stage

Under both effective P_d values, specimens treated with 50%H_2 and 100%H_2 show smaller maximum ε_v than the specimens treated with 0% H_2. Past studies have reported contradicting relationships between φ and compressibility (changes in the pore volume with respect to the change in pore pressure under a specific confining pressure) [30]. Hall [31] and Newman [32] proposed negative relationships between φ and compressibility from experiments on sandstone samples from different reservoirs. Fatt [33] reported no relationship for sandstone reservoir samples, collected from 7 different reservoirs. On the other hand, Ceia et al. [34] showed a positive relationship between φ and compressibility for Berea and Boise sandstone samples. The experimental results conclude that the lower compressibility of specimens treated with hydrogen cannot totally be attributed to porosity, but the mineralogy of the specimens could play an important role. Quartz grains are harder and brittle, and carbonate and clay minerals are quite weak and ductile [35]. When P_d is applied to the specimen, the carbonate and clay grains will experience higher deformation than quart grains. Hence, specimens treated with hydrogen, containing higher quartz and lower carbonate and clay minerals as shown in Table 2, experience lower ε_v than specimens treated with 0%H_2.

4.3. Axial loading stage

4.3.1. Axial stress-strain responses

Fig. 9a shows the plots of the deviatoric stress ($\Delta\sigma_d$) versus the axial strain (right side of the plot) and radial strain (left side of the plot) from the UC tests for the four rock specimens. Specimen S7 (50H-UC) exhibits a uniaxial compressive strength (UCS) value of 80 MPa, 27% lower than the UCS of specimen S4 (0H-UC). Similarly, the UCS value of the specimen S10 (100H-UC) is 72 MPa, 34% lower than that of the specimen S4 (0H-UC). Furthermore, a decreasing trend of UCS values was observed from 0% H_2 to 100% H_2 treatment. The specimen S10 (100H-UC) fails at a higher axial strain of about 10 mε, compared to that of all other specimens. All the specimens have a similar brittle failure behavior with a sudden drop in axial stress. For quantifying the failure behavior of the specimens, the brittleness index (BI) suggested by Tarasov & Potvin [36] given by Eq. (6) was used.

$$BI = \frac{E}{M} \tag{6}$$

where E is the elastic modulus of the pre-peak region and M is the elastic modulus of the post-peak region in the stress-strain plot, and a higher BI value indicates a more ductile behavior. Fig. 10 compares the BI values with the P_d for all specimens. All the UC specimens similarly show brittle failure behavior with BI values ranging from 0.07 to 0.42.

Fig. 9b shows the deviatoric stress ($\Delta\sigma_d$) versus the axial strain (right side of the plot) and radial strain (left side of the plot) from the TC tests under a P_c of 43 MPa and a P_p of 23 MPa (or P_d = 20 MPa). The specimens S2 (0H-TC20) and S5 (0H-TC20) have a maximum compressive strength of about 164 MPa. Interestingly, specimen S8 (50H-TC20) shows a slightly higher strength of about 169 MPa. Probably due to the heterogeneity of the specimen, the effect of 50%H_2-treatment cannot be realized. However, the specimen S11 (100H-TC20) shows 43% decrease in the compressive strength than that of the 0%H_2-treated specimens.

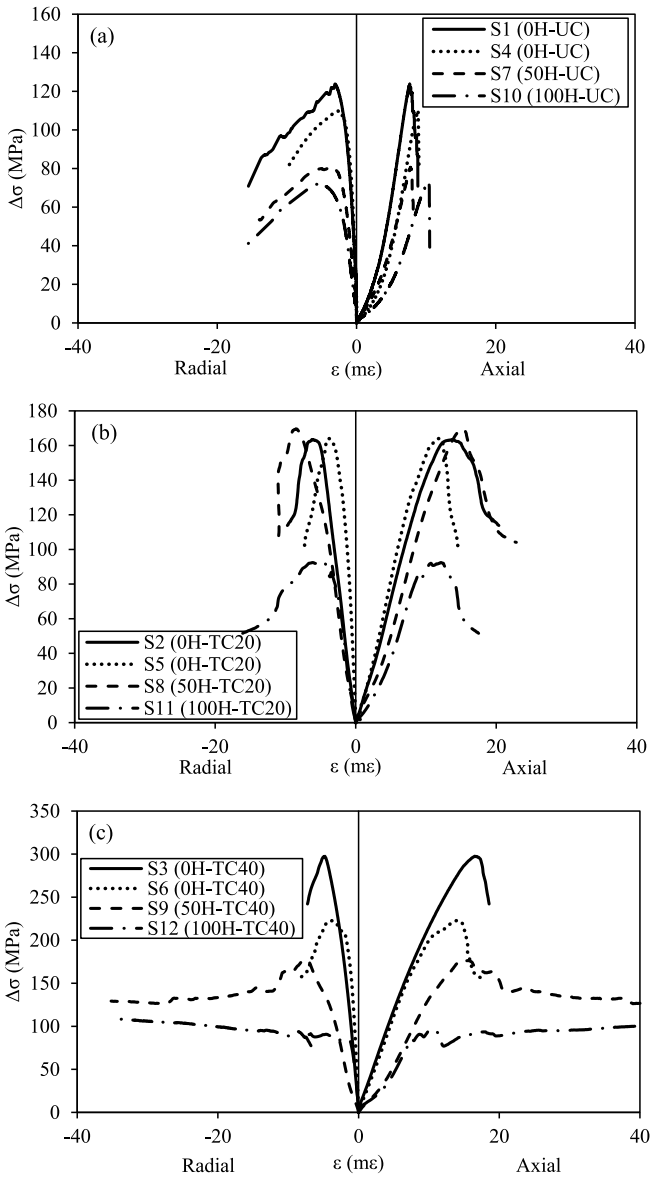

Fig. 9. The changes in the deviatoric stress ($\Delta\sigma_d$) versus the axial strain (right side of the plot) and radial strain (left side of the plot) in the a) UC tests, b) TC test under an effective confining pressure of 20 MPa, and c) TC test under an effective confining pressure of 40 MPa.

The axial strains at their corresponding maximum strengths are comparable. Because of the effect of P_d, the axial stress-strain responses of all four specimens do not exhibit a sudden decrease in axial stress as observed in the UC tests. Fig. 10 shows that specimen S11 (100H-TC20) has a higher BI of 1.1 than the BI = 0.7 of specimen S5 (0H-TC20). However, specimen S8 (50H-TC20) showed 52% lower BI value, compared to the BI = 1.46 of specimen S5 (0H-TC20). A comparison between the BI = 1.74 of specimen S2 (0H-TC20) and the BI = 0.7 of specimen S5 (0H-TC20) indicates that higher porosity increases the brittleness. The post-failure behaviors are comparable with a gradual decrease in the axial stresses with an increase in axial strain. The responses show that the hydrogen treatment probably does not have much effect on the failure mode of the specimens under the P_d of 20 MPa.

Fig. 9c shows the deviatoric stress ($\Delta\sigma_d$) versus the axial strain (right side of the plot) and radial strain (left side of the plot) from the TC tests under a P_c of 63 MPa and a P_p of 23 MPa (or P_d = 40 MPa). The specimen S3 (0H-TC40) exhibits a larger maximum strength of 297 MPa than the maximum strength of 223 MPa of the S6 (0H-TC40). The specimen S9

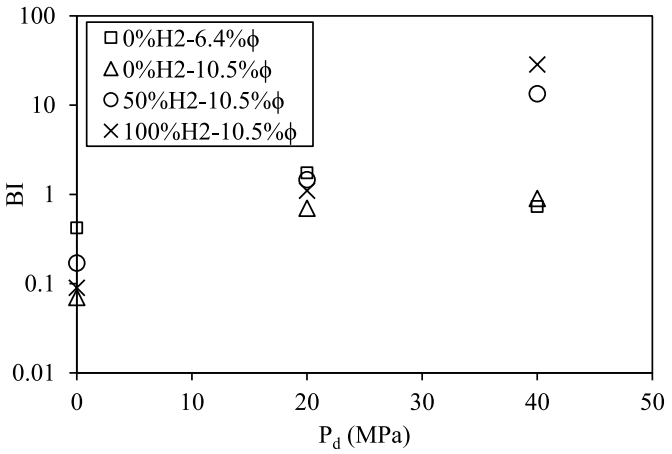

Fig. 10. The relationship between the brittleness index (BI) and the P_d for all the specimens.

(50H-TC40) shows a 3% lower maximum strength of 217 MPa than that of the S6 (0H-TC40). Further, the specimen S12 (100H-TC40) shows 58% and 56% lower maximum strength of 95 MPa than that of the specimens S6 (0H-TC40) and S9 (50H-TC40). Therefore, the responses show that increasing the H_2 treatment from 0% to 100% reduces the maximum compressive strength. The specimens S6 (0H-TC40) and S9 (50H-TC40) fail at an axial strain of 15 mε while specimen S12 (100H-TC40) fails at a lower axial strain of 11 mε. The responses show that increasing the hydrogen concentration reduces the axial strain at the maximum strength. Fig. 9c shows that specimen S9 treated with 50%H_2 and specimen S12 treated with 100%H_2 fail in a more ductile manner. Fig. 10 confirms that specimens S9 (50H-TC40) and S12 (100H-TC40) exhibit higher BI values of 13.4 and 28.5, respectively, than the BI = 0.9 of specimen S6 (0H-TC40).

4.3.2. *Relationship between microstructure and mechanical behavior in axial loading stage*

Under all P_d values, the specimens treated with hydrogen show lower compressive strengths than those of the specimens treated with 0%H_2, and the compressive strength decreases with the increase in percent hydrogen. This effect can be attributed to two reasons: 1) effect of porosity: Fig. 6 shows that the porosity was increased by the hydrogen treatment and percent of hydrogen. Hence, the H_2-treated specimens with higher φ indicating higher void spaces experience lower compressive strength under triaxial compression conditions [37], and 2) effect of mineral composition: Table 3 shows that H_2-treated specimens have lower carbonate and clay contents, which imply weaker cementation between quartz particles. Hence, lower stress is needed to generate crack propagation [38], and lower shear resistance is available during the TC test.

4.3.3. *Elastic properties*

Fig. 11a–b shows the elastic modulus (E) and Poisson's ratio (ν) versus the P_d, respectively, for all the specimens. In each stress-strain curve (Fig. 9a–c), a linear portion was determined between the crack closure stress threshold and 50% of the peak strength for each specimen, and the slope of the linear portion was calculated as the E. The crack closure threshold is defined as the stress level at which the closure of pre-existing cracks during the initial stage of loading happens, which was described using the method proposed by Yu et al. [39]. The ν was calculated for the same linear portion of the stress-strain curve.

Fig. 11a shows that the E increases with the increase in P_d for all the specimens. Under the UC condition ($P_d = 0$), the two specimens treated with 0%H_2 (S1 and S4) show a comparable E of 15 GPa despite their slight difference in φ. A larger difference in E of about 3 GPa is observed for the specimens treated with 0%H_2 at P_d = 20 MPa; however, the difference diminishes at P_d = 40 MPa. For all P_d, the E values decrease with the increase in H_2 from 0% to 100%. Under the UC condition, compared to the E of specimens treated with 0%H_2, the E values of the specimens treated with 50%H_2 and 100%H_2 decrease by 23% and 37%, respectively. For P_d of 20 MPa, the E = 14 GPa of the specimen S8 (50H-TC20) and E = 10 GPa of the specimen S11 (100H-TC20) are 28% and 48% lower than the E = 19 GPa of the specimen S5 (0H-TC20), respectively. Likewise, For P_d of 40 MPa, the E = 16 GPa of the specimen S9 (50H-TC40) and E = 13 GPa of the specimen S12 (100H-TC40) are 28% and 43% lower than E = 22.89 GPa of the specimen S6 (0H-TC40), respectively.

Fig. 11b shows the comparison of ν and P_d for all the specimens. Increasing the P_d from 0 to 20 MPa increases the ν for all the treatment conditions. This could be due to the softening effect from the P_d of 20 MPa. Continuous increase in P_d from 20 to 40 MPa decreases the ν for all the specimens. Higher confinement can provide a higher restraint against deformations, resulting in lower ν values. For the UC condition, specimens S1 (0H-UC) and S4 (0H-UC) have the lowest ν of about 0.05 while specimens S7 (50H-UC) and S10 (100H-UC) have similar ν of about 0.15. The H_2 treatment tends to soften the rock specimen and increase the ν. However, for P_d of 20 MPa, specimens S2 (0H-TC20) and S8 (50H-TC20) show a similar ν of about 0.4. Specimen S11 (100H-TC20) shows a higher ν of about 0.28 or 67% higher than that of specimen S5 (0H-TC20). For P_d of 40 MPa, specimens S6 (0H-TC40) and S12 (100H-TC40) show a similar ν of about 0.1 while specimen S9 (50H-TC40) has a higher ν of about 0.4.

4.3.4. *Major effective principal stress or maximum compressive strength*

Fig. 12 compares the major effective principal stress (P'_a) as the summation of the peak deviatoric stress ($\Delta\sigma_d$) and P_d given by Eq. (7)

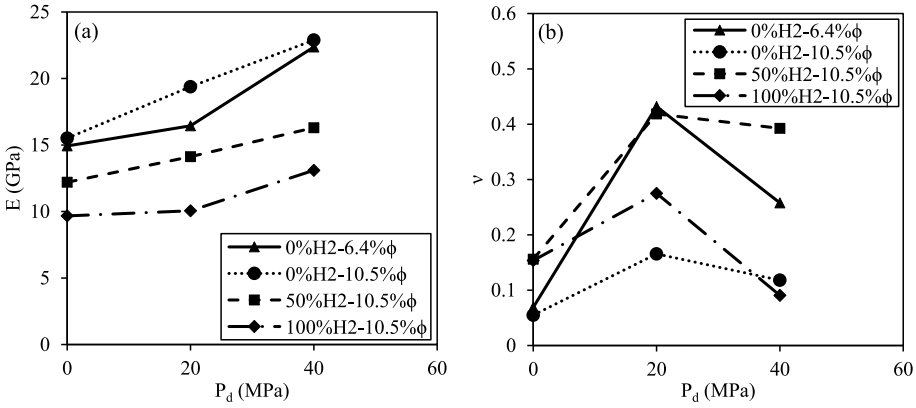

Fig. 11. Changes in a) the elastic modulus, and b) Poisson's ratio versus the effective confining pressure for all the specimens.

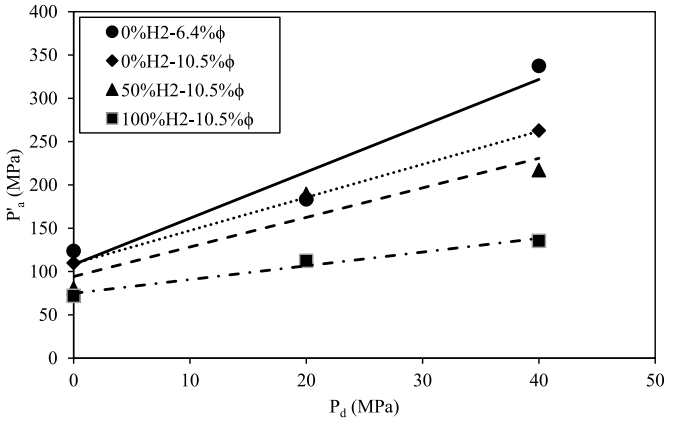

Fig. 12. The comparison of the major effective principal stress (P'_a) and minor effective principal stress (P_d) of all the specimens.

$$P'_a = P_d + \Delta\sigma_d \tag{7}$$

In all cases, increasing the P_d increases the P'_a of the specimens. However, the increment of P'_a varies with the treatment conditions. The P'_a of specimens treated with 0%H_2 with φ of 6.4% increases 21% from P_d = 0–20 MPa and 121% from 0 to 40 MPa. Likewise, the P'_a of specimens treated with 0%H_2 with φ of 10.5% increases by 73% from P_d = 0–20 MPa and 140% from 0 to 40 MPa. However, for the same 0%H_2 treatment condition, the specimens with a lower φ of 6.4% indicating lower pore spaces exhibit higher P'_a values than those with φ of 10.5%. For the specimens treated with 50%H_2, the P'_a values at P_d of 20 and 40 MPa are 110 and 120% higher than that of the specimen tested under the UC condition, respectively. For the specimens treated with 100%H_2, the P'_a values at P_d of 20 and 40 MPa are 28 and 32% higher than that of the specimen tested under UC condition. Comparing the percent increase in the P'_a, specimens treated with 100%H_2 experience the smallest increase in P'_a with the P_d.

Fig. 12 also shows that the P'_a envelope of specimens treated with 0% H_2 reduces up to 35% when the φ increases from 6.4 to 10.5%. The 50% H_2 treatment further reduces the P'_a envelope with the reduction varying between 17 and 35%. The greatest reduction in P'_a envelope ranging from 35 to 49% is realized on specimens treated with 100%H_2. This comparison of P'_a envelopes clearly shows the negative effect of hydrogen on the P'_a of Hulett sandstone specimens.

4.3.5. *Shear strength parameters*

Table 4 compares the shear strength parameters in terms of the effective friction angle (φ′) and the effective cohesion (c') of the specimens with different treatment conditions. The φ′ was calculated using Eq. (8) in terms of the gradient (*a*) of the linear P'_a envelope line with respect to P_d (Fig. 12). The c' was calculated using Eq. (9) in terms of φ′ and the y-axis intercept (*b*) of the linear P'_a envelope line.

$$\varphi' = \sin^{-1}\left(\frac{a-1}{a+1}\right) \tag{8}$$

$$c' = \frac{b(1-\sin\varphi')}{2\cos\varphi'} \tag{9}$$

Table 4 shows that the specimens treated with 0%H_2 with φ of 6.4% have the highest φ′ of about 43°, and the specimens treated with 100%H_2 have the lowest φ′ of 13°. Increasing the φ of the specimens treated with 0%H_2 from 6.4 to 10.5% reduces the φ′ from 43° to 35°. The 50%H_2 treatment reduces the φ′ from 43° to 33° or by 23%. Increasing the concentration of H_2 treatment to 100% greatly reduces the φ′ from 36° to 13° or by 63%. On the other hand, the effect of H_2 treatment on c' cannot be distinctly observed as the c' ranges from 23 to 30 MPa for the different treatment conditions, and minimal differences were observed due to H_2 treatment.

Table 4
The c' and φ' for all the specimens.

Parameter	0%H_2-6.4%φ	0%H_2-10.5%φ	50%H_2-10.5%φ	100%H_2-10.5%φ
φ' (°)	43.21	35.82	33.14	13.11
c' (MPa)	23.38	27.9	25.51	29.72

5. Conclusions

The effect of hydrogen treatment on the properties and behavior of sandstone specimens was investigated in this study. The following conclusions are drawn:

1) XRD shows a relative increase in the weight percent of quartz and an associated decrease in dolomite and clay minerals after treatment with hydrogen. BET results show a slight increase in total pore volume and surface area of the specimens treated with hydrogen. SEM images show that specimens treated with hydrogen have larger pores and smoother surfaces.
2) The hydrogen treatment decreases the maximum volumetric strain during the confining stage. For P_d = 40 MPa, the specimens treated with 50%H_2 and 100%H_2 show 31% and 80% smaller maximum volumetric strains than that of the specimen treated with 0%H_2.
3) At higher P_d, the effect of hydrogen on the peak strength of specimens is more pronounced. Compared to the specimens treated with 0%H_2, the specimens treated with 100%H_2 showed 34, 43, and 58% lower peak strength under the UC, TC (P_d = 20 MPa), and TC (P_d = 40 MPa) conditions, respectively. Specimens treated with 50%H_2 experience 35, 0, and 40% lower peak strengths, respectively.
4) Although specimens treated with hydrogen mostly failed at a smaller axial strain, they failed in a more ductile manner. From the UC to TC at P_d = 20 MPa test condition, specimens treated with hydrogen show an increase in ductility. Under the TC at P_d = 40 MPa, the specimens treated with hydrogen show more ductile behavior than the specimens treated with 0%H_2.
5) For P_d = 40 MPa and comparing with the E of the specimen treated with 0%H_2, the 50%H_2 and 100%H_2 treatments decrease the E values of specimens by 28% and 43%, respectively. The effect of hydron on Poisson's ratio depends on the P_d. For the UC and TC at P_d = 20 MPa conditions, the specimens treated with 100%H_2 exhibit 200 and 67% higher Poisson's ratios than that of the specimen treated with 0%H_2. However, for the TC at P_d = 40 MPa, the specimens treated with 100%H_2 exhibit 24% lower Poisson's ratio.
6) Treating the specimens with 50%H_2 and 100%H_2 decreases the effective friction angles by 23% and 63%, respectively. However, the effect of hydrogen on the effective cohesion cannot be distinctly observed.

Declaration of competing interest

The authors declare that they have no known competing financial interests or personal relationships that could have appeared to influence the work reported in this paper.

Acknowledgement

The authors would like to acknowledge the funding support from the Hydrogen Energy Research Center, School of Energy Resources of the University of Wyoming. The authors also like to thank the Materials Characterization Laboratory and Geochemistry Analytical Laboratory at the University of Wyoming for the services provided.

References

[1] Al-Yaseri A, Esteban L, Yekeen N, Giwelli A, Sarout J, Sarmadivaleh M. The effect of clay on initial and residual saturation of hydrogen in clay-rich sandstone formation: implications for underground hydrogen storage. Int J Hydrogen Energy 2023;48(13):5175–85. https://doi.org/10.1016/j.ijhydene.2022.11.059.

[2] Thiyagarajan SR, Emadi H, Hussain A, Patange P, Watson M. A comprehensive review of the mechanisms and efficiency of underground hydrogen storage. Journal of energy storage, vol. 51. Elsevier Ltd; 2022. https://doi.org/10.1016/j.est.2022.104490.

[3] IEA. Net zero by 2050. Paris: IEA; 2021. https://www.iea.org/reports/net-zero-by-2050. License: CC BY 4.0.

[4] Gbadamosi AO, Muhammed NS, Patil S, Al Shehri D, Haq B, Epelle EI, Mahmoud M, Kamal MS. Underground hydrogen storage: a critical assessment of fluid-fluid and fluid-rock interactions. J Energy Storage 2023;72. https://doi.org/10.1016/j.est.2023.108473. Elsevier Ltd.

[5] Yates E, Bischoff A, Beggs M, Jackson N. Hydrogen geostorage in aotearoa/New Zealand hydrocarbons associated with buried volcanoes view project impacts of magmatism on the evolution of sedimentary basins view project hydrogen geo-storage in aotearoa-New Zealand. 2021. https://doi.org/10.13140/RG.2.2.27113.21603.

[6] IEA. Global hydrogen review 2021. Paris: IEA; 2021. https://www.iea.org/reports/global-hydrogen-review-2021. License: CC BY 4.0.

[7] Zivar D, Kumar S, Foroozesh J. Underground hydrogen storage: a comprehensive review. Int J Hydrogen Energy 2021;46(45):23436–62. https://doi.org/10.1016/j.ijhydene.2020.08.138.

[8] Muhammed NS, Haq B, Al Shehri D, Al-Ahmed A, Rahman MM, Zaman E. A review on underground hydrogen storage: insight into geological sites, influencing factors and future outlook. Energy Rep 2022;8:461–99. https://doi.org/10.1016/j.egyr.2021.12.002. Elsevier Ltd.

[9] Sainz-Garcia A, Abarca E, Rubi V, Grandia F. Assessment of feasible strategies for seasonal underground hydrogen storage in a saline aquifer. Int J Hydrogen Energy 2017;42(26):16657–66. https://doi.org/10.1016/j.ijhydene.2017.05.076.

[10] Mahdi DS, Al-Khdheeawi EA, Yuan Y, Zhang Y, Iglauer S. Hydrogen underground storage efficiency in a heterogeneous sandstone reservoir. Advan. Geo-Energy Res. 2021;5(4):437–43. https://doi.org/10.46690/ager.2021.04.08.

[11] Singh H. Hydrogen storage in inactive horizontal shale gas wells: techno-economic analysis for Haynesville shale. Appl Energy 2022;313. https://doi.org/10.1016/j.apenergy.2022.118862.

[12] Truche L, Jodin-Caumon MC, Lerouge C, Berger G, Mosser-Ruck R, Giffaut E, Michau N. Sulphide mineral reactions in clay-rich rock induced by high hydrogen pressure. Application to disturbed or natural settings up to 250°C and 30bar. Chem Geol 2013;351:217–28. https://doi.org/10.1016/j.chemgeo.2013.05.025.

[13] Henkel S, Pudlo D, Werner L, Enzmann F, Reitenbach V, Albrecht D, Würdemann H, Heister K, Ganzer L, Gaupp R. Mineral reactions in the geological underground induced by H2 and CO2 injections. Energy Proc 2014;63:8026–35. https://doi.org/10.1016/j.egypro.2014.11.839.

[14] Flesch S, Pudlo D, Albrecht D, Jacob A, Enzmann F. Hydrogen underground storage—petrographic and petrophysical variations in reservoir sandstones from laboratory experiments under simulated reservoir conditions. Int J Hydrogen Energy 2018;43(45):20822–35. https://doi.org/10.1016/j.ijhydene.2018.09.112.

[15] Pudlo D, Flesch S, Albrecht D, Reitenbach V. The impact of hydrogen on potential underground energy reservoirs. Geophysical Research abstracts, vol. 20; 2018.

[16] Yekta AE, Pichavant M, Audigane P. Evaluation of geochemical reactivity of hydrogen in sandstone: application to geological storage. Appl Geochem 2018;95:182–94. https://doi.org/10.1016/j.apgeochem.2018.05.021.

[17] Hassanpouryouzband A, Adie K, Cowen T, Thaysen EM, Heinemann N, Butler IB, Wilkinson M, Edlmann K. Geological hydrogen storage: geochemical reactivity of hydrogen with sandstone reservoirs. ACS Energy Lett 2022;7(7):2203–10. https://doi.org/10.1021/acsenergylett.2c01024.

[18] Gelencsér O, Árvai C, Mika LT, Breitner D, LeClair D, Szabó C, Falus G, Szabó-Krausz Z. Effect of hydrogen on calcite reactivity in sandstone reservoirs: experimental results compared to geochemical modeling predictions. J Energy Storage 2023;61. https://doi.org/10.1016/j.est.2023.106737.

[19] Quillinan S, McLaughlin J, Coddington K. Commercial-scale carbon storage complex feasibility study at dry fork station, Wyoming. 2021. https://doi.org/10.2172/1780712.

[20] Spencer CW. Hydrocarbon generation as a mechanism for overpressuring in Rocky Mountain region. AAPG (Am Assoc Pet Geol) Bull 1987;71(4):368–88.

[21] Pan P, Wu Z, Feng X, Yan F. Geomechanical modeling of CO 2 geological storage: a review. J Rock Mech Geotech Eng 2016;8(6):936–47. https://doi.org/10.1016/j.jrmge.2016.10.002.

[22] Royal Society T. Locked away – geological carbon storage: policy briefing. the Royal Society; 2022.

[23] Schmitt RR, Andrews GDM, Moore J, Paronish T, Workman S, Gumowski LM, Brown SR, Crandall D, Neubaum J. Self-sealing mafic sills for carbon and hydrogen storage. Geol. Soc., London, Special Pub. 2023;528(1):359–76. https://doi.org/10.1144/SP528-2022-43.

[24] Yu Y, Farzana S, Nye C, Bagdonas D, Waghmare PR, Jiao Z, McLaughlin JF. Wettability variation and its impact on CO2 storage capacity at the Wyoming CarbonSAFE storage hub: an experimental approach. Fuel 2023;344:128111. https://doi.org/10.1016/j.fuel.2023.128111.

[25] Drever JI. The preparation of oriented clay mineral specimens for X-ray diffraction analysis by a filter-membrane peel technique. Am Mineral: J. Earth Planet. Mater. 1973;58(5–6):553–4.

[26] Mock K, Amato J, Bertmaring J. GeoPixelCounter [software]. Retrieved from, http://www.math.uaa.alaska.edu/~afkjm/GeoPixelCounter/; 2012. Version 1.0.

[27] Al-Yaseri A, Al-Mukainah H, Yekeen N, Al-Qasim AS. Experimental investigation of hydrogen-carbonate reactions via computerized tomography: implications for underground hydrogen storage. Int J Hydrogen Energy 2023;48(9):3583–92. https://doi.org/10.1016/j.ijhydene.2022.10.148.

[28] Hemme C, van Berk W. Hydrogeochemical modeling to identify potential risks of underground hydrogen storage in depleted gas fields. Appl Sci 2018;8(11):2282. https://doi.org/10.3390/app8112282.

[29] Labus K, Tarkowski R. Modeling hydrogen – rock – brine interactions for the Jurassic reservoir and cap rocks from Polish Lowlands. Int J Hydrogen Energy 2022;47(20):10947–62. https://doi.org/10.1016/j.ijhydene.2022.01.134.

[30] Lyons WC. Basic principles, definitions, and data. In: Working guide to reservoir engineering. Elsevier; 2010. p. 1–95. https://doi.org/10.1016/B978-1-85617-824-2.00001-0.

[31] Hall HN. Compressibility of reservoir rocks. J Petrol Technol 1953;5(1):17–9. https://doi.org/10.2118/953309-G.

[32] Newman GH. Pore-volume compressibility of consolidated, friable, and unconsolidated reservoir rocks under hydrostatic loading. J Petrol Technol 1973;25(2):129–34. https://doi.org/10.2118/3835-PA.

[33] Fatt I. Pore volume compressibilities of sandstone reservoir rocks. J Petrol Technol 1958;10(3):64–6. https://doi.org/10.2118/970-G.

[34] Ceia M, Missagia R, Fasolo R, Neto I. Relationship between porosity, permeability and pore compressibility. Proc. 16th Int. Congress Brazilian Geophys. Soc. Expogef 2019:1–6. https://doi.org/10.22564/16cisbgf2019.287.

[35] Hu Y, Guo Y, Qing H, Hou Y. Study on influencing factors and mechanism of pore compressibility of tight sandstone reservoir—a case study of upper carboniferous in ordos basin. Front Earth Sci 2023;10. https://doi.org/10.3389/feart.2022.1100951.

[36] Tarasov B, Potvin Y. Universal criteria for rock brittleness estimation under triaxial compression. Int J Rock Mech Min Sci 2013;59:57–69. https://doi.org/10.1016/j.ijrmms.2012.12.011.

[37] Qi Y, Ju Y, Yu K, Meng S, Qiao P. The effect of grain size, porosity and mineralogy on the compressive strength of tight sandstones: a case study from the eastern Ordos Basin, China. J Petrol Sci Eng 2022;208:109461. https://doi.org/10.1016/j.petrol.2021.109461.

[38] Guo S, Pu H, Yang M, Liu D, Sha Z, Xu J. Study of the influence of clay minerals on the mechanical and percolation properties of weakly cemented rocks. Geofluids 2022:1–15. https://doi.org/10.1155/2022/1712740. 2022.

[39] Yu H, Ng K, Grana D, Kaszuba J, Alvarado V, Campbell E. Experimental investigation of the effect of compliant pores on reservoir rocks under hydrostatic and triaxial compression stress states. Can Geotech J 2019;56(7):983–91. https://doi.org/10.1139/cgj-2018-0133. 6.